



# Effect of microstructure variation on corrosion properties of as-cast 0Cr23Ni13 stainless steel at high strain rate of hot compression

Jun-chen Li<sup>1</sup> · Meng-yuan Ye<sup>2</sup> · Rui-dong Li<sup>1</sup> · Xing-run Chen<sup>3</sup>

Received: 12 July 2022 / Revised: 23 August 2022 / Accepted: 29 August 2022 / Published online: 22 March 2023  
© China Iron and Steel Research Institute Group Co., Ltd. 2023

## Abstract

The optimization of hot compression technique of as-cast 0Cr23Ni13 stainless steel at high strain rate was discussed, and its corrosion resistance was evaluated after hot compression treatment experimentally. By adjusting the dynamic recrystallization (DRX) ratio of 0Cr23Ni13 stainless steel during hot pressing, the content of low  $\Sigma$  coincident site lattice ( $\Sigma$ CSL) grain boundaries is increased, and the grain orientation is optimized. The results show that ferrite and austenite are completely recrystallized at 1050 and 1150 °C, respectively. The number of grains in the  $\langle 111 \rangle$  and  $\langle 101 \rangle$  directions increases significantly, the corrosion potential increases, and the corrosion current density decreases, which will significantly improve the corrosion resistance of 0Cr23Ni13 stainless steel. After the optimization of grain boundary distribution, corrosion resistance is noticeably improved due to the existence of low  $\Sigma$ CSL boundaries. The interference effect of low  $\Sigma$ CSL grain boundary on random grain boundary network becomes intense with the increase in DRX ratio, which is the fundamental measure to improve the corrosion resistance.

**Keywords** 0Cr23Ni13 stainless steel · Hot compression · Dynamic recrystallization · Low  $\Sigma$  coincident site lattice · Corrosion resistance

## 1 Introduction

0Cr23Ni13 steel contains high Ni and Cr contents, ultra-low carbon content, and  $\sim 10\%$  ferrite. Because of high Ni and Cr contents, it not only has excellent plasticity, toughness, and corrosion resistance at room temperature, but also can improve the oxidation resistance and creep strength at high temperature. Therefore, it is widely used in the petrochemical, heating furnace, boiler, and industrial furnace industries [1–4]. Although 0Cr23Ni13 stainless steel has good corrosion resistance in air, water, and various oxidizing media, different degrees of corrosion may still occur in some harsh environments [5–9]. It has been

previously reported that the corrosion resistance is directly related to the internal microstructure, grain boundaries (GBs) distribution and interfacial energy storage of metal materials [10–13]. Austenitic stainless steel has almost no phase transformation during hot compression. It is considered that recrystallization is the key factor affecting its final microstructure [14, 15]. In the process of hot compression, recrystallization not only improves the internal microstructure morphology of the metal materials, but also optimizes the distribution of the GBs characteristics, which improves the corrosion resistance of material to a certain extent [16–19]. Jia et al. [20] found that a large number of low  $\Sigma$  coincident site lattice ( $\Sigma$ CSL) boundaries dominated by twinning boundaries ( $n = 1, 2, 3$ ) would be generated with the occurrence of dynamic recrystallization (DRX). This phenomenon can improve the creep strength, intergranular corrosion resistance, and stress corrosion resistance of the material. Arafin and Szpunar [21] reported that low angle and special CSL boundaries exhibited crack-resistance, while the CSL boundaries beyond  $\Sigma 13b$  and the random high angle boundaries were prone to crack. Shi et al. [22] studied the intergranular corrosion behavior of

✉ Jun-chen Li  
lijunchen605@163.com

<sup>1</sup> School of Material Science and Engineering, Lanzhou University of Technology, Lanzhou 730050, Gansu, China

<sup>2</sup> Xi'an Hantang Analysis and Testing Co., Ltd., Xi'an 710201, Shaanxi, China

<sup>3</sup> Jiuquan Iron and Steel (Group) Co., Ltd., Jiayuguan 735100, Gansu, China

18Mn18Cr0.63N and found that boundaries beyond  $\Sigma 3$  showed no corrosion. A previous study found that low  $\Sigma$ CSL boundaries exhibited superior corrosion resistance as compared to randomly distributed high angle grain boundaries (HAGBs) [23]. Gertsman and Bruemmer [24] reported that the boundaries beyond  $\Sigma 3$ ,  $\Sigma 9$ , and  $\Sigma 27$  had good corrosion resistance. The low  $\Sigma$ CSL boundaries had a good inhibition effect on the corrosion properties of materials. And a high proportion of low  $\Sigma$ CSL boundaries exhibited a good protection effect on austenitic stainless steel. Some scholars argued that random GBs were susceptible to corrosion, whereas most of the CSL GBs (mainly  $\Sigma 3$  and  $\Sigma 9$ ) exhibited better resistance to corrosion [25–27]. This paper aims to establish the relationship between compression temperature and microstructure to predict the effects of grain size, dynamic recrystallization, and low  $\Sigma$ CSL boundaries ratios on the corrosion properties of 0Cr23Ni13 stainless steel at different temperatures.

## 2 Experimental

The stainless steel specimens used in this study were prepared from a cast ingot, with the chemical composition of C 0.018, Si 0.36, Mn 1.84, P 0.013, S 0.0005, Ni 13.80, Cr 23.21, Cu 0.02, N 0.062, and Fe balance (wt.%). Cylindrical specimens with the size of  $\phi 10$  mm  $\times$  15 mm were prepared from the ingot via machining and were subjected to isothermal compression tests on a Gleeble-3500 thermal simulator (Beijing, China). The specimens were heated to compression temperature and held for 180 s to generate a uniform microstructure. The overall height reduction in compression was set to 50% at compression temperatures ranging from 950 to 1250 °C and  $10$  s<sup>-1</sup>. After compression, the specimens were quenched in water to preserve the microstructure. The specimens were wire-cut after hot compression along the compression direction (CD), and half of the specimens were collected to prepare the metallographic samples. Microstructure variation in the specimen center was examined using an Olympus PMG 613U optical microscope (OM). The original microstructure is

shown in Fig. 1a (white is austenite, and gray is ferrite). The other half of the specimens were prepared by electrolytic polishing in 10% HClO<sub>4</sub> + 90% C<sub>2</sub>H<sub>5</sub>OH. The electronic backscattering probe (AZTECX-MAX80) equipped on the LEO-1450 scanning electron microscope (SEM) was used for electron backscatter diffraction (EBSD) analysis with a voltage of 15 kV and a step size of 1  $\mu$ m. The position of the EBSD scanning area is shown in Fig. 1d, where ND was the normal direction of the compression surface, and TD was the landscape direction. The hot compression specimens at different compression temperatures were tested in a corrosive solution of 87% H<sub>2</sub>O + 10% HNO<sub>3</sub> + 3% HF. And the samples were taken out every 12 h for cleaning, drying, and weighing. The CHI604C electrochemical workstation was used for electrochemical measurement of different samples in 3.5% NaCl solution at 25 °C. The test system was composed of three traditional electrodes: a 0Cr23Ni13 stainless steel working electrode, a platinum plate auxiliary electrode, a saturated calomel electrode as the reference electrode, and a working electrode with an exposed area of 1 cm<sup>2</sup>.

## 3 Results and discussion

### 3.1 Hot compression results and microstructure

The average grain size changes of 0Cr23Ni13 stainless steel at a strain rate of  $10$  s<sup>-1</sup> and a compression temperature range of 950–1250 °C are illustrated in Fig. 2. The stress–strain curve shows a gradual decrease in flow stress with the increase in compression temperature. At the initial stage of compression, the stress increases sharply with a small increase in strain variables, and the phenomenon of work hardening begins to appear. The continuous increase in strain variables fluctuates to the steady-state region, which represents a balance between work hardening, dynamic recovery (DRV), and DRX. The microstructure indicates that the average ferrite grain size in 0Cr23Ni13 stainless steel slightly increases with increasing compression temperature, and the average grain size of austenite

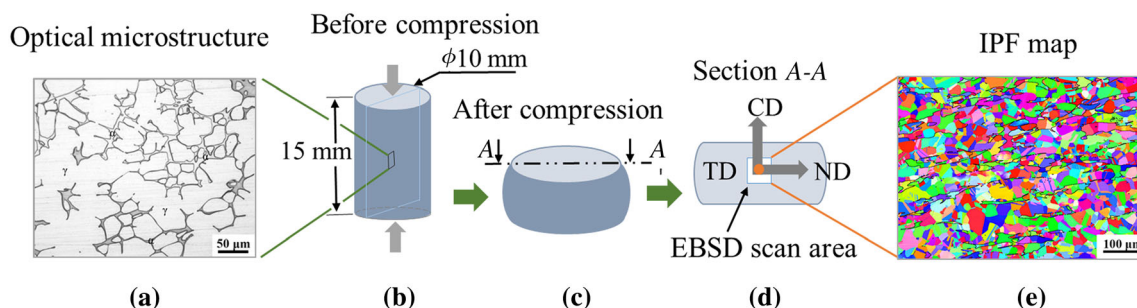
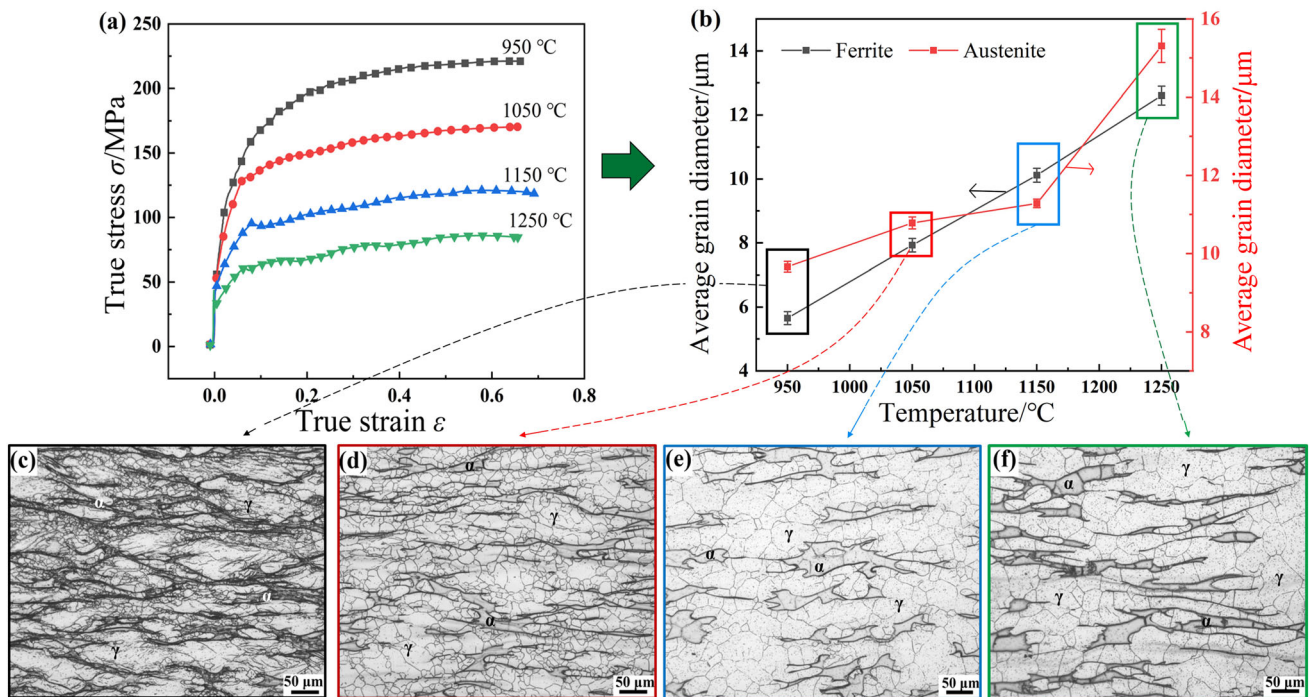


Fig. 1 Schematic representation of compression specimens. IPF—Inverse pole figure



**Fig. 2** Average grain size of 0Cr23Ni13 stainless steel at different compression temperatures. **a** Stress–strain curve; **b** average grain size; **c** 950 °C; **d** 1050 °C; **e** 1150 °C; **f** 1250 °C

increases obviously with the increase in compression temperature. At the compression temperature of 950 °C (Fig. 2c), new austenite recrystallized grains start to form at bulging GBs, and the average grain size of ferrite has been measured to be 5.66  $\mu\text{m}$ . Due to the formation of fine austenite recrystallized grains, the size of original coarse austenite is reduced, and the average austenite grain size is measured as 9.66  $\mu\text{m}$ . As the compression temperature rises to 1050 °C (Fig. 2d), newly formed fine austenite recrystallized grains are increasingly generated. At this time, the average size of austenite grains is measured as 10.78  $\mu\text{m}$ , and the average size of ferrite grains is increased to 8.47  $\mu\text{m}$ . At the compression temperature of 1150 °C (Fig. 2e), the average grain size of ferrite increases to 10.36  $\mu\text{m}$ , and the newly formed austenite grains continue to grow and homogenize, generating an average grain size of 11.28  $\mu\text{m}$ . When the compression temperature reaches 1250 °C (Fig. 2f), the compression at high strain rate will cause an adiabatic heating effect on the stainless steel. Under the high strain rate, the time required for the sample to deform to the height of the experimental setting is only 0.2 s, and the heat cannot diffuse out in a very short time during the deformation, resulting in an increase of 19 °C in the internal temperature of the sample. This leads to further growth of the average grain size. Therefore, the migration rate of GBs and the grain growth rate rapidly increase. The average austenite grain size then expeditiously increases to 15.31  $\mu\text{m}$ , while the average ferrite grain size increases to

13.84  $\mu\text{m}$ . Overall, the average grain size of ferrite in 0Cr23Ni13 stainless steel rises with the increase in compression temperature. The austenite microstructure maintains its original coarse shape at lower temperatures ( $< 1050$  °C), and a small amount of recrystallized grains are observed. At medium and high temperatures ( $\geq 1050$  °C), the degree of recrystallization is enhanced by the gradual increase in compression temperature. Obvious changes of the microstructure are observed, and the average grain size also gradually increases at the same time.

When the material is deformed, the microstructure variation is mainly caused by the presence of DRX in the material, which affects the orientation distribution, size, and morphology of the grains and GBs [28, 29]. The EBSD images of 0Cr23Ni13 stainless steel at the strain rate of  $10 \text{ s}^{-1}$  and the compression temperature range of 950–1250 °C are shown in Fig. 3. As can be seen from the recrystallization diagram in Fig. 3e–h, the degree of recrystallization is highly dependent on the temperature. At a compression temperature of 950 °C, ferrite exhibits an obvious DRX degree, and the proportion of recrystallization is measured as 64.2%. Combined with Fig. 2c, austenite recrystallization only starts at this time and presents a recrystallization proportion of 11.92%. There is 88.3% ferrite DRX at 1050 °C, indicating almost complete recrystallization. And the austenite DRX rapidly increases to 39.2%. At a compression temperature of 1150 °C, a minimal recrystallization percentage is observed. The grain

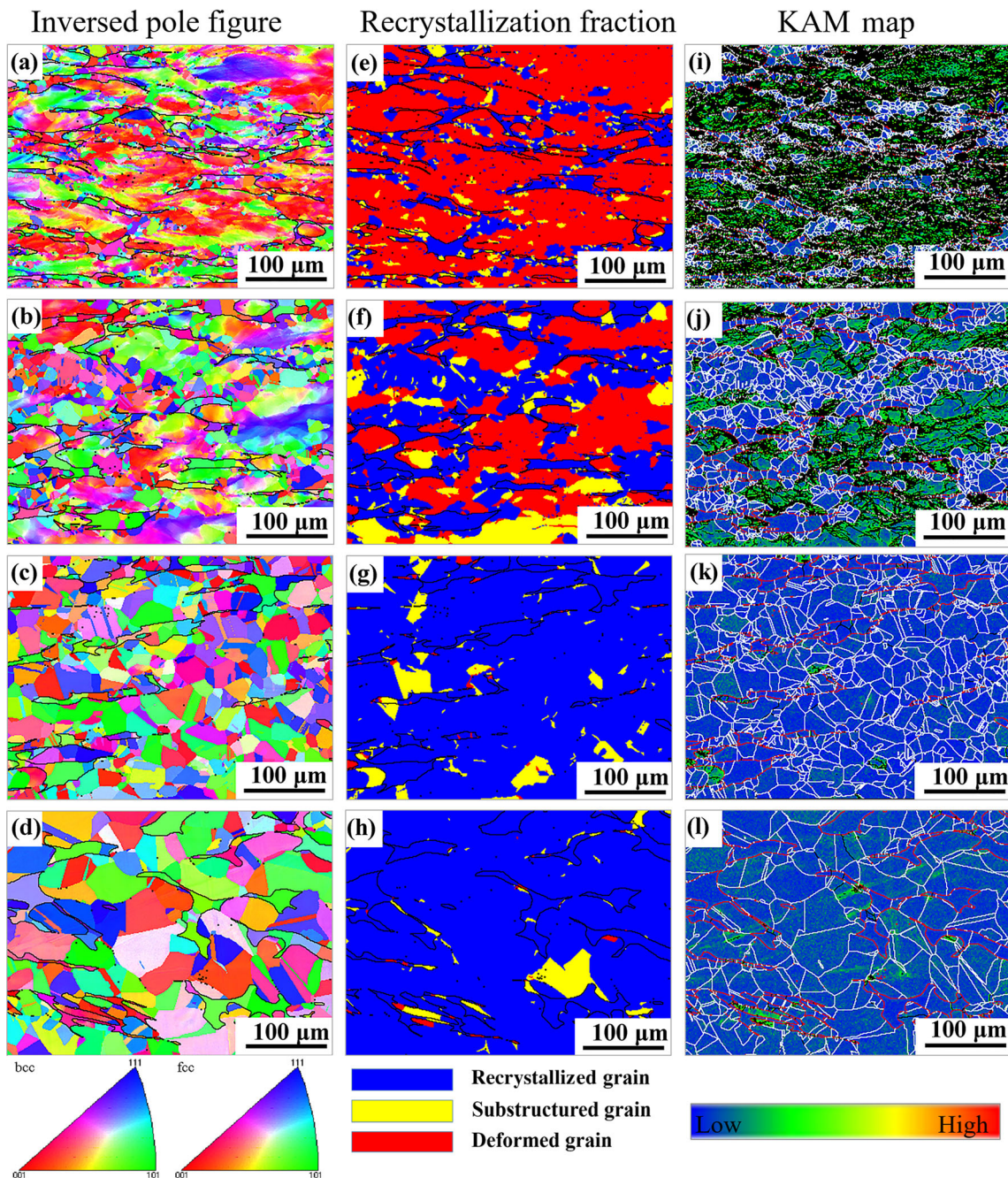


**Fig. 3** EBSD images of 0Cr23Ni13 stainless steel at strain rate of  $10 \text{ s}^{-1}$  and different temperatures. **a–d** Grain orientation map; **e–h** recrystallization distribution map; **i–l** kernel average misorientation

(KAM) map. Red, black, and white lines represent phase boundaries, boundaries with angle of  $2^\circ$ – $15^\circ$ , and boundaries with angle above  $15^\circ$ , respectively

size continues to grow, and the ferrite tends to be almost completely recrystallized. At this time, the DRX degree of austenite reaches its maximum, and the proportion of recrystallization reaches up to 93.3%. As shown in Fig. 2e, the newly formed fine austenite recrystallized grains generate new austenite equiaxed grains. At this point, the grains formed by DRX completely replace the large grains, suggesting that the DRX process can be enhanced by

increasing the temperature. At a compression temperature of  $1250 \text{ }^\circ\text{C}$ , minimal changes in the degree of ferrite DRX are observed, whereas austenite DRX slightly decreases to 92.1% due to the positive correlation between the DRV capability and compression temperature. This consumes part of the distortion energy generated by compression and reduces the driving force for DRX occurrence, thus reducing the proportion of DRX. At higher experimental

temperatures, the DRX of ferrite and austenite gradually intensifies. The ferrite is almost completely recrystallized at 1050 °C, while austenite is completely recrystallized at 1150 °C.

In the kernel average misorientation map, the average misorientation is higher in the process of low-temperature compression, and it decreases at higher compression temperature. When the sample deformed at low temperature (Fig. 3i), more dislocation aggregations are observed at the low-angle grain boundaries (LAGBs), and dislocations recombine through motion to create dislocation cells. Then, the dislocation cells are developed into subgrains. At higher compression temperature, the subgrains continuously absorb dislocations, resulting in DRX phenomenon. The subgrains gradually change from LAGBs to HAGBs. As seen in Fig. 3i–l, with the gradual increase in the deformation temperature, the dislocation density gradually decreases. This is because 0Cr23Ni13 stainless steel will produce subgrains structures of LAGBs during the hot deformation process. These subgrains structures will continuously absorb the movable dislocations inside the grains, thereby reducing the dislocation density. This shows that DRX is more fully carried out.

### 3.2 Hot compression results and low $\Sigma$ CSL boundaries

Low stacking fault energy metals tend to undergo dynamic recrystallization during hot deformation. During the process of recrystallization and nucleation, the original grain boundary is bowed due to inhomogeneous deformation. The grain boundary bow region is formed by the gradual development of subgrain boundaries or the generation of twin grain boundaries to form recrystallized nuclei, and the nuclei grow to form twin crystals. Due to the low content of ferrite with high-level stacking fault energy in 0Cr23Ni13 stainless steel, the effect of engineering modification based on grain boundary engineering is poor, and low  $\Sigma$ CSL boundaries are not easily formed during hot deformation. Therefore, this paper mainly analyzes the influence of the change of low  $\Sigma$ CSL boundaries content in austenite during hot deformation on corrosion properties. Figure 4 shows the variation of low- and high-angle GBs ratio and  $\Sigma$ 3 twin boundaries content of 0Cr23Ni13 stainless steel at a strain rate of  $10 \text{ s}^{-1}$  and a compression temperature range of 950–1250 °C. A large number of studies show that the  $\Sigma$ 3 twin boundaries can effectively improve the corrosion resistance of alloy and reduce the corrosion rate of austenitic stainless steel [20, 30, 31]. The peak values of the samples at different compression temperatures are observed at boundaries angle  $\theta = 2^\circ\text{--}5^\circ$  in Fig. 4. At higher compression temperatures, the misorientation of the austenite GBs gradually changes to a larger

range of  $\theta = 30^\circ\text{--}60^\circ$ , and a relatively high peak value is observed at  $\theta = 60^\circ$ . In austenitic stainless steel,  $\theta = 60^\circ$  corresponds to the  $\Sigma$ 3 twin boundaries interface, indicating that a large number of  $\Sigma$ 3 twin boundaries are formed in the austenitic phase [31]. At low temperature (Fig. 4a), LAGBs with high density are mainly enriched in austenite. However, DRX is observed in ferrite, and the misorientation of the ferrite GBs gradually transits to a high-angle range of  $\theta = 15^\circ\text{--}60^\circ$ , which is conducive to HAGBs formation. When the compression temperature is 1050 °C (Fig. 4b), the content of HAGBs increases with the continuous increase in DRX in austenite. At the higher temperature stage with relatively complete DRX (Fig. 4c), the content of LAGBs rapidly decreases, and the misorientation of the austenite GBs changes to a high-angle range of  $\theta = 30^\circ\text{--}60^\circ$ . New HAGBs are formed at the original sites, and the content of  $\Sigma$ 3 twin boundaries rapidly increases to 38.8%. When the compression temperature rises to 1250 °C (Fig. 4d), LAGBs transforms into HAGBs, and  $\Sigma$ 3 twin boundaries reaches a maximum of 42.5%. During the process of recrystallization and nucleation, the original grain boundary is bowed due to inhomogeneous deformation. The grain boundary bow region is formed by the gradual development of subgrain boundaries or the generation of twin grain boundaries to form recrystallized nuclei, and the nuclei grow to form twin crystals. That is to say, the grain boundary content of low  $\Sigma$ CSL increases with the gradual increase in the degree of dynamic recrystallization.

The low  $\Sigma$ CSL boundaries have a great influence on the corrosion performance. Because the low  $\Sigma$ CSL interface energy can stabilize its property, produce less impurity segregation and reduce its mobility, the increase in low  $\Sigma$ CSL boundaries content significantly improves the corrosion resistance of stainless steel [10, 32–34]. Figure 5 shows that the  $\Sigma$ 3 GBs of 0Cr23Ni13 stainless steel play a dominant role in the hot compression process as compared to the  $\Sigma$ 9 and  $\Sigma$ 27 GBs at different compression temperatures. The austenite DRX mechanism is triggered at 950 °C (Fig. 5a), and it generates a small amount of low  $\Sigma$ CSL boundaries, which is about 2.42%. Severe corrosion is observed at the original austenite GBs, which results in the generation of continuous corrosion pits. At a compression temperature of 1050 °C (Fig. 5b), the austenite DRX is intensified, and a large number of recrystallized grains are generated. In addition, discontinuous corrosion pits are generated around the GBs of the recrystallized grains. At this point, the low  $\Sigma$ CSL boundaries have a proportion of about 8.10%. At a compression temperature of 1150 °C (Fig. 5c), the austenite has been almost completely recrystallized, and the proportion of low  $\Sigma$ CSL boundaries rapidly increases to 41.35%. It is obvious from Fig. 5 that the  $\Sigma$ 3 GBs have good corrosion resistance, and almost all twins are not corroded. At a compression

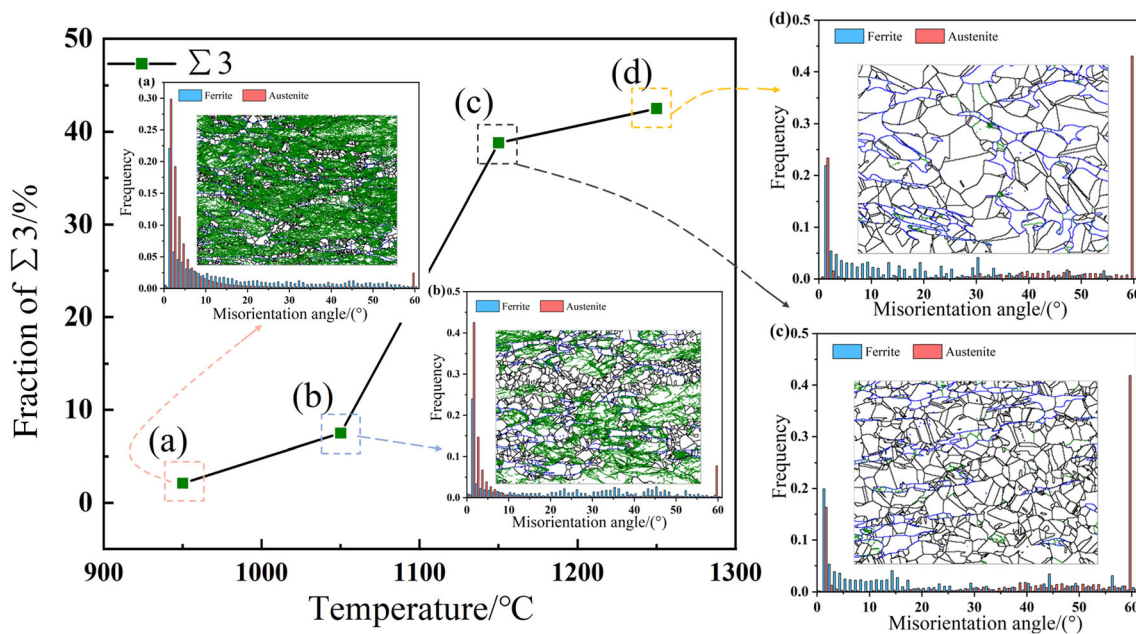


**Fig. 4**  $\Sigma 3$  twin boundaries and misorientation angle content variation of 0Cr23Ni13 stainless steel at strain rate of  $10 \text{ s}^{-1}$  for 950 °C (a), 1050 °C (b), 1150 °C (c), and 1250 °C (d). Sky blue and peach lines

represent ferrite and austenite, respectively. Green and black lines represent boundaries with angle of  $2^\circ$ – $15^\circ$  and boundaries with angle above  $15^\circ$ , respectively

temperature of 1250 °C, the low  $\Sigma$ CSL boundaries are evenly distributed when DRX is completed (Fig. 5d). With the continuous growth of recrystallized grains, the  $\Sigma 3$  GBs continue to extend, and the proportion of low  $\Sigma$ CSL boundaries reaches 44.60%. Meanwhile, Fig. 5 also shows that with the gradual increase in compression temperature, the low  $\Sigma$ CSL boundaries lead to the interruption of intergranular network, the connectivity of HAGBs network is reduced, and the corrosion behavior is inhibited. These results indicate that the content of low  $\Sigma$ CSL boundaries plays an important role in improving the corrosion resistance of 0Cr23Ni13 stainless steel.

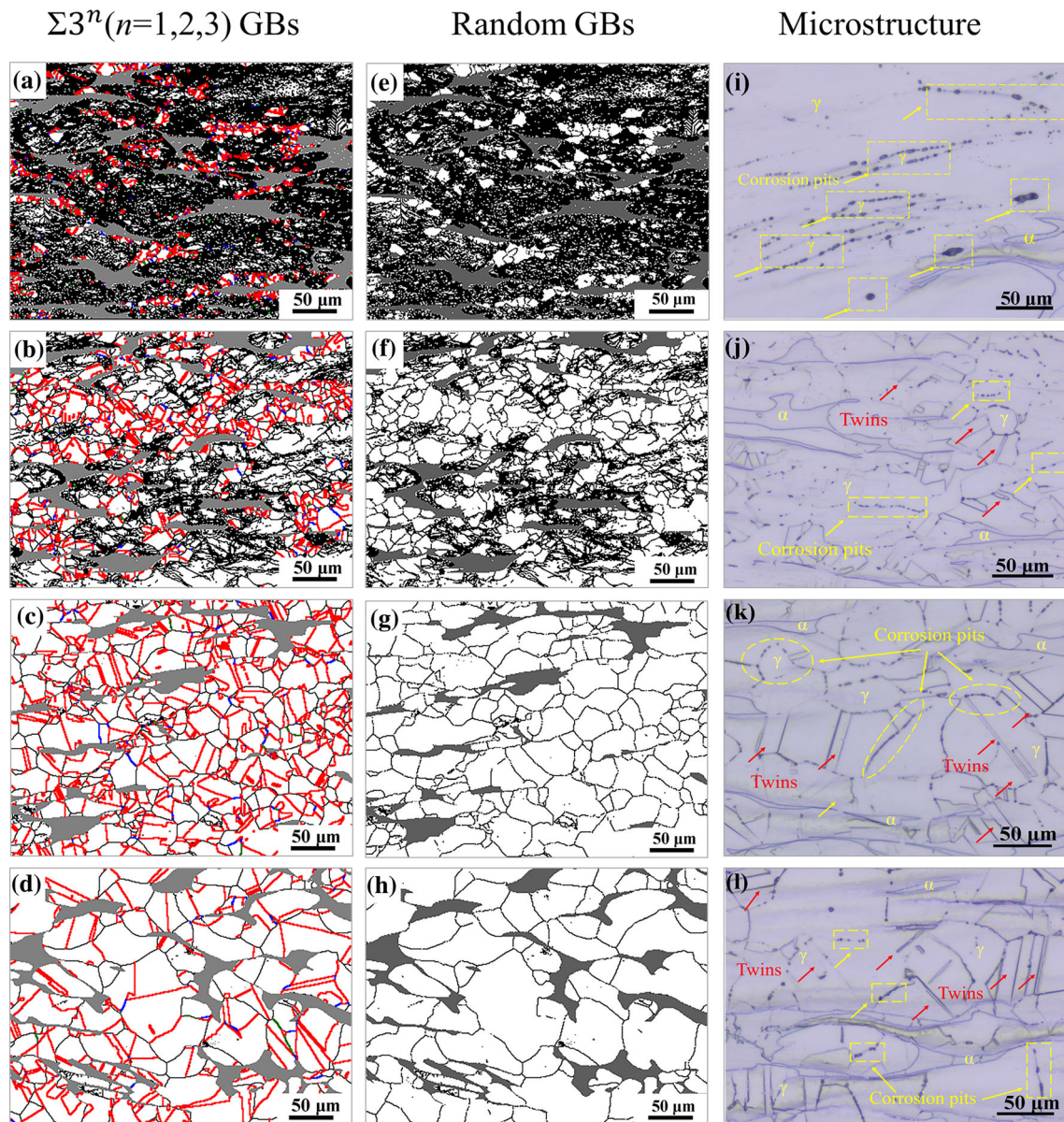
The results of electrochemical test at different compression temperatures in the 3.5 wt.% NaCl solution are shown in Fig. 6. The experimental results show that the polarization curves of 0Cr23Ni13 stainless steel are similar, and the corresponding passivation current density is very small, indicating that the surface of stainless steel has been passivated. A dense layer of passivation film is formed on the surface of the sample, which hinders the reaction between the sample and the corrosive liquid [35]. The corrosion current density is almost constant with the increase in potential. As the corrosion potential continues to increase, the current density suddenly increases, the passivation film breaks, and the corrosion of stainless steel is observed.

Table 1 shows the electrochemical parameters of the samples with different low  $\Sigma$ CSL boundaries ratios calculated from the polarization curves. In the electrochemical

experiments, the corrosion resistance of metal is reflected by the corrosion potential and corrosion current density. Greater corrosion potential values are less prone to corrosion, and smaller corrosion current density values indicate better corrosion resistance [36, 37]. According to Table 1, the increase in the low  $\Sigma$ CSL boundaries results in the increase in the overall corrosion potential of 0Cr23Ni13 stainless steel and a decrease in corrosion current density. In addition, the average austenite grain size does not change much at 950–1250 °C, while the proportion of low  $\Sigma$ CSL boundaries rapidly increases from 2.39% to 44.62%. The content of low  $\Sigma$ CSL boundaries varies greatly, indicating that the content of low  $\Sigma$ CSL boundaries is the main factor affecting corrosion at the compression temperature of 950–1250 °C. At a compression temperature of 1250 °C, the 0Cr23Ni13 stainless steel exhibits the largest grain size, the lowest number of micro-batteries formed in the unit area is observed, the maximum corrosion potential value is measured at  $-0.370 \text{ V}$ , and the minimum corrosion current density is measured to be  $2.842 \times 10^{-6} \text{ A cm}^{-2}$ .

### 3.3 Effect of microstructure on corrosion properties of 0Cr23Ni13 stainless steel

As shown in Fig. 3e–h, the degree of recrystallization is also sensitive to the deformation temperature. With the gradual increase in the compression temperature, the degree of dynamic recrystallization gradually increases, and the microstructure of 0Cr23Ni13 stainless steel



**Fig. 5** Low  $\Sigma$ CSL boundaries of 0Cr23Ni13 stainless steel at a strain rate of  $10 \text{ s}^{-1}$  and different temperatures. **a–d** 950–1250 °C (Shaded areas represent ferrite. Red, green, and blue lines represent  $\Sigma 3$ ,  $\Sigma 9$ ,

and  $\Sigma 27$  boundaries, respectively); **e–h** random boundaries; **i–l** corrosion microstructure

changes significantly. Meanwhile, the grains gradually become uniform, the average grain size gradually increases, and the grains align at preferred orientation. The number of grains in the  $\langle 111 \rangle$  and  $\langle 101 \rangle$  directions increases significantly. In addition, it can be found from Fig. 4 that higher  $\Sigma 3$  boundaries proportion will be generated due to the continuous increase in compression temperature, when the compression temperature is below 1150 °C. This is because when the main mechanism in compression is nucleation, the content of  $\Sigma 3$  twin boundaries increases with the enhancement of DRX, indicating that DRX promotes the formation of  $\Sigma 3$  twin boundaries.

When the compression temperature is above 1250 °C, DRX has been basically completed. The main mechanism of compression is grain growth, and the  $\Sigma 3$  boundaries increase further with the continuous elongation of  $\Sigma 3$  boundaries generated by DRX, which is also consistent with previous research in Inconel 625 alloy [38].

In the IPF, the grain is rotated with the enhancement in DRX (Fig. 3e–h). The grains are aligned on the preferred orientation in 0Cr23Ni13 stainless steel. With the increasing degree of DRX, the number of grain orientations in the  $\langle 111 \rangle$  and  $\langle 101 \rangle$  directions increased significantly. As a result, the corrosion resistance of the material

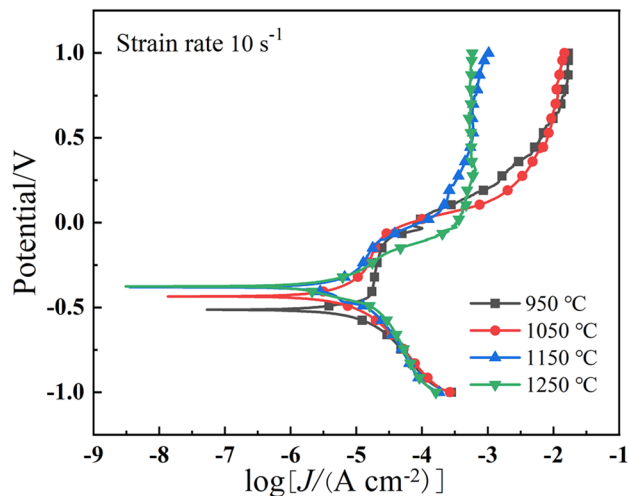


**Fig. 6** Polarization curves in NaCl solution of 0Cr23Ni13 stainless steel at a strain rate of  $10 \text{ s}^{-1}$ .  $J$ —Current density

**Table 1** Parameters related to polarization curve of 0Cr23Ni13 stainless steel

Temperature/ °C	Average grain size/ $\mu\text{m}$	Low $\Sigma\text{CSL}$ / %	Corrosion potential/ V	Corrosion current density/ ( $\text{A cm}^{-2}$ )
950	9.66	2.39	- 0.507	$7.858 \times 10^{-6}$
1050	10.78	8.20	- 0.425	$6.549 \times 10^{-6}$
1150	11.28	41.37	- 0.372	$4.723 \times 10^{-6}$
1250	15.31	44.62	- 0.370	$2.842 \times 10^{-6}$

is gradually enhanced. Austenitic stainless steel is a typical face-centered cubic (FCC) lattice metal, (101) and (111) are compact planes of FCC atoms, and the (001) plane is sub-compact plane of atoms. Among the three typical low index crystal planes, the one near (001) plane is the most sensitive to corrosion points, whereas (111) and (101) exhibit strong resistance to corrosion points. It can be seen from Fig. 6 combined with Table 1 that with the increase in the dense surface in 0Cr23Ni13 stainless steel, its corrosion potential gradually increases, and its corrosion current density gradually decreases. Therefore, the corrosion resistance of the material can be improved by increasing the number of grain orientation in the  $\langle 111 \rangle$  and  $\langle 101 \rangle$  directions, which is also similar with previous research in 304 austenitic stainless steel [28].

### 3.4 Effect of low $\Sigma\text{CSL}$ boundaries on corrosion properties of 0Cr23Ni13 stainless steel

Figure 7 shows the change of the corrosion mass loss and microstructure of 0Cr23Ni13 stainless steel at different compression temperatures. As can be seen from Fig. 7, the mass loss gradually decreases with the increase in different

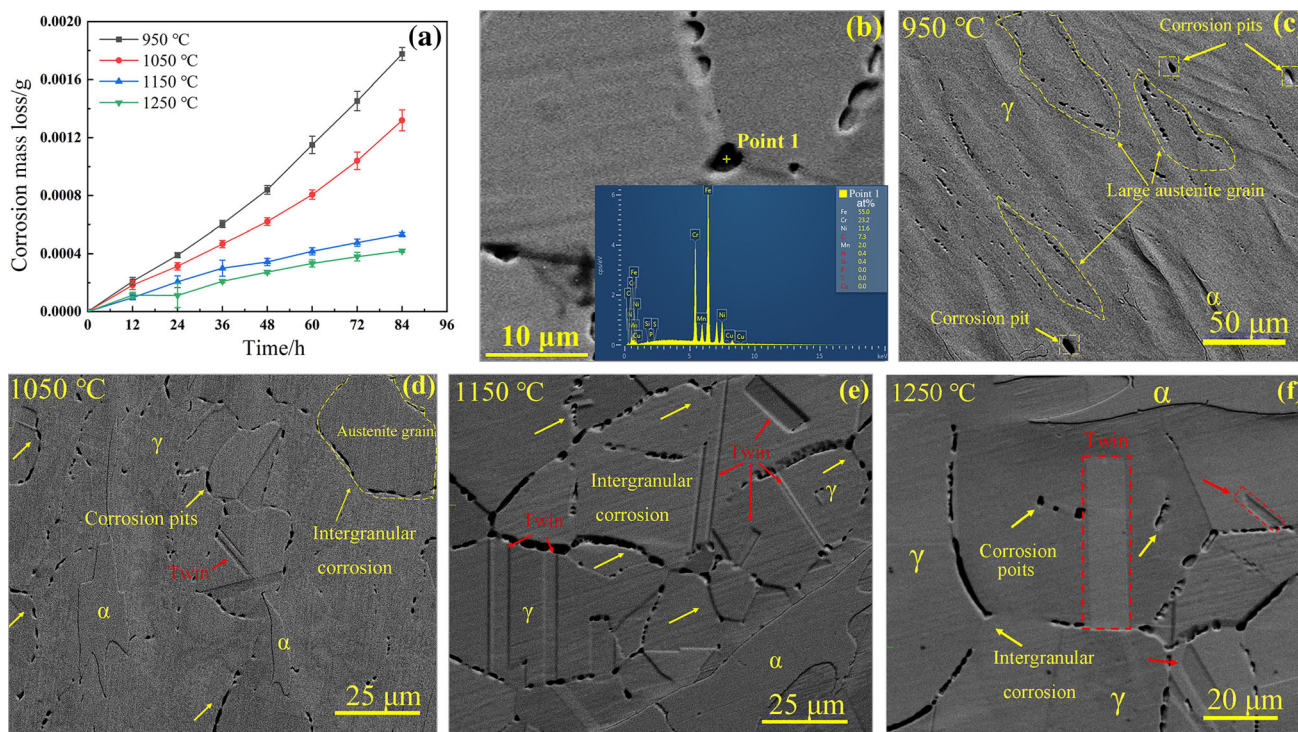
temperatures, indicating that corrosion resistance depends on the content of low  $\Sigma\text{CSL}$  boundaries. Discontinuous corrosion pits are observed around the austenite GBs, and the energy spectrum shows that continuous  $\text{Cr}_{23}\text{C}_6$  compounds are precipitated at the austenite GBs. The experimental results are similar to those observed by Ningshen and Mudali [39]. In the process of carbide precipitation, the diffusion rate of C is much higher than that of Cr in austenite. As a result, the Cr content consumed near GBs could not be replenished by elemental diffusion on time, such that the Cr content near the GBs was lower than the minimum content required for passivation (12 wt.%), thus forming a chromium-depleted zone near the GBs [12, 40]. This mechanism leads to an electrochemical difference between the GBs region and the grain, which forms an active and blunt micro-battery, and finally leads to corrosion occurrence. Meanwhile, it can be seen from Fig. 7f that low-energy twins can effectively block the connectivity of random GBs. When the material is corroded, the corrosion spreads to the inner part of the matrix along the random GBs. When the low  $\Sigma\text{CSL}$  boundaries are encountered, the corrosion can be blocked to the matrix, so as to prevent the corrosion.

Figure 8 schematically shows the hindering of corrosion penetration from the surface to the interior by low  $\Sigma\text{CSL}$  boundaries distributed in the network of random GBs. In the experimental steel, the degree of DRX of austenite increases, with the increase in the number of twins in the recrystallized grains, leading to an increase in the low  $\Sigma\text{CSL}$  boundaries. It is obvious from Fig. 5i–l that the low  $\Sigma\text{CSL}$  boundaries have good corrosion resistance, and almost all twins are not corroded. As shown in Fig. 8, the low  $\Sigma\text{CSL}$  boundaries produced in the random GBs network by DRX ways promote the disconnection of the random GBs network, which hinders the penetration of corrosion from surface into the interior and significantly improves corrosion resistance of the steel. Due to electrochemical differences between GBs regions and grains, which form an active and blunt micro-battery, it can be seen from Fig. 7f and Table 1 that when the deformation temperature is 1250 °C, the average grain size of 0Cr23Ni13 stainless steel is the largest, and the number of corrosion micro-batteries formed in a unit area is the least, resulting in the weakest effect of corrosion.

## 4 Conclusions

1. The average grain size of ferrite and austenite gradually increases with the increase in compression temperature in the process of hot compression at the strain rate of  $10 \text{ s}^{-1}$ . The degree of recrystallization is sensitive to the deformation temperature. Ferrite and





**Fig. 7** Mass loss change of 0Cr23Ni13 stainless steel at strain rate of  $10 \text{ s}^{-1}$ . **a** Mass loss map; **b** energy spectrum map; **c** 950 °C; **d** 1050 °C; **e** 1150 °C; **f** 1250 °C

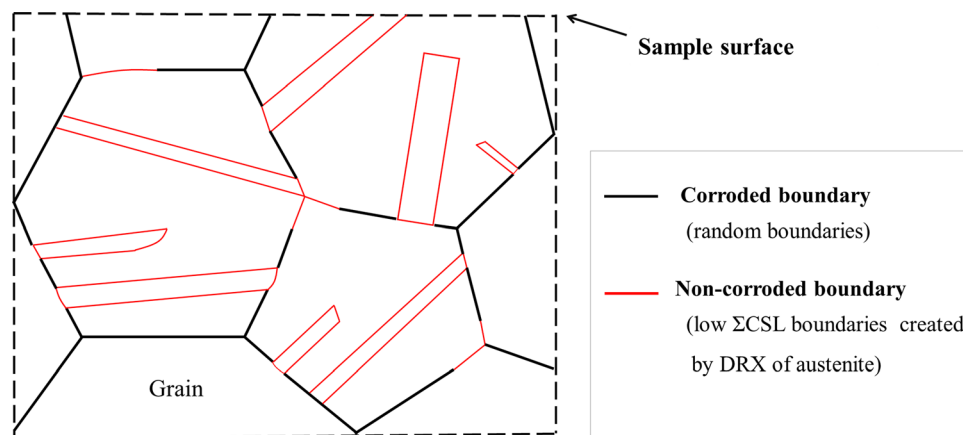


**Fig. 8** Schematic diagram showing hindering of corrosion penetration from surface into interior by low  $\Sigma$ CSL boundaries distributed in random grain boundaries network

austenite recrystallize completely at 1050 and 1150 °C, respectively.

2. The number of grains aligned in the  $\langle 111 \rangle$  and  $\langle 101 \rangle$  directions increases significantly with the gradual increase in DRX, which significantly improves the corrosion resistance of 0Cr23Ni13 stainless steel.
3. The low  $\Sigma$ CSL boundaries increase with the gradual increase in DRX. The increase in low  $\Sigma$ CSL boundaries greatly reduces the connectivity of the random boundary network and optimizes GBs distribution,

which is the essential reason for the improvement of corrosion resistance.

**Acknowledgements** This research was financially supported by the Science and Technology Major Project of Gansu Province (Grant No. 17ZD2GB012) and the City Key Research and Development Plan of Jiayuguan (Grant Nos. 20-16). The authors are also grateful for the technical assistance from the State Key Laboratory of Advanced Processing and Recycling of Nonferrous Metals, Lanzhou University of Technology.

## Declarations

**Conflict of interest** The authors have no relevant financial or non-financial interests to disclose.

## References

- [1] Z. Zhuo, S. Xia, Q. Bai, B. Zhou, *J. Mater. Sci.* 53 (2018) 2844–2858.
- [2] S. Rahimi, D.L. Engelberg, T.J. Marrow, *Mater. Sci. Technol.* 26 (2010) 670–675.
- [3] M.S. Ghazani, B. Eghbali, G. Ebrahimi, *Met. Mater. Int.* 23 (2017) 964–973.
- [4] X. Lou, M. Song, P.W. Emigh, M.A. Othon, P.L. Andresen, *Corros. Sci.* 128 (2017) 140–153.
- [5] G. Yamada, H. Kokawa, Y. Yasuda, S. Tokita, T. Yokoyama, Y.S. Sato, H.T. Fujii, *Philos. Mag.* 93 (2013) 1443–1453.
- [6] M.C. Bignozzi, L. Calcinelli, M. Carati, L. Ceschini, C. Chiavari, G. Masi, A. Morri, *Met. Mater. Int.* 26 (2020) 1318–1328.
- [7] V. Firouzdor, K. Sridharan, G. Cao, M. Anderson, T.R. Allen, *Corros. Sci.* 69 (2013) 281–291.
- [8] Z.B. Zheng, J. Long, Y. Guo, H. Li, K.H. Zheng, Y.X. Qiao, *J. Iron Steel Res. Int.* 29 (2022) 1853–1863.
- [9] J. Yang, Z.B. Wang, Y.X. Qiao, Y.G. Zheng, *Corros. Sci.* 199 (2022) 110210.
- [10] J. Gao, J. Tan, X. Wu, S. Xia, *Corros. Sci.* 152 (2019) 190–201.
- [11] J. Lei, J. Xie, S. Zhou, H. Song, X. Song, X. Zhou, *Opt. Laser Technol.* 111 (2019) 271–283.
- [12] J. Qi, B. Huang, Z. Wang, H. Ding, J. Xi, W. Fu, *J. Mater. Sci. Technol.* 33 (2017) 1621–1628.
- [13] B. Zwa, Z. Bing, *Mater. Des.* 212 (2021) 109496.
- [14] A. Dehghan-Manshadi, M.R. Barnett, P.D. Hodgson, *Mater. Sci. Eng. A* 485 (2008) 664–672.
- [15] A.N. Belyakov, R.O. Kaibyshev, *Met. Sci. Heat. Treat.* 34 (1992) 324–329.
- [16] S. Yang, Z.J. Wang, H. Kokawa, Y.S. Sato, *J. Mater. Sci.* 42 (2007) 847–853.
- [17] S.Y.W. Huang, L. Chai, L. Jiang, H. Liu, F. Wang, D. Wang, J. Wang, *Met. Mater. Int.* 25 (2019) 364–371.
- [18] W. Kingkam, C.Z. Zhao, L. Hong, H.X. Zhang, Z.M. Li, *Acta Metall. Sin. (Engl. Lett.)* 32 (2019) 495–505.
- [19] Y. Yang, S. Li, in: 2012 International Conference on Chemical Engineering, Hongkong, China, 2012, pp. 1054–1057.
- [20] Z. Jia, Z. Gao, J. Ji, D. Liu, T. Guo, Y. Ding, *Eng. Mater.* 21 (2019) 1900426.
- [21] M.A. Arafin, J.A. Szpunar, *Corros. Sci.* 51 (2009) 119–128.
- [22] F. Shi, P.C. Tian, N. Jia, Z.H. Ye, Y. Qi, C.M. Liu, X.W. Li, *Corros. Sci.* 107 (2016) 49–59.
- [23] D. An, T.A. Griffiths, P. Konijnenberg, S. Mandal, Z. Wang, S. Zaefferer, *Acta Mater.* 156 (2018) 297–309.
- [24] V.Y. Gertsman, S.M. Bruemmer, *Acta Mater.* 49 (2001) 1589–1598.
- [25] X.Y. Fang, W.G. Wang, H. Guo, X. Zhang, B.X. Zhou, *J. Iron Steel Res. Int.* 14 (2007) No. S1, 339–343.
- [26] I. Samajdar, P. Ahniedavadi, D.N. Wasnik, *Mater. Sci.* 495–497 (2005) 453–458.
- [27] C. Hu, X. Shuang, L. Hui, T. Liu, B. Zhou, W. Chen, W. Ning, *Corros. Sci.* 53 (2011) 1880–1886.
- [28] G.Z. Quan, G.C. Luo, J.T. Liang, D.S. Wu, A. Mao, Q. Liu, *Comp. Mater. Sci.* 97 (2015) 136–147.
- [29] M.S. Chen, Y.C. Lin, X.S. Ma, *Mater. Sci. Eng. A* 556 (2012) 260–266.
- [30] J.L. Sun, H.T. Zhou, L. Chen, H. Wu, W.L. Liu, F. Yao, Y.L. Xu, *J. Mater. Res.* 34 (2020) 231–240.
- [31] N. Sakaguchi, Y. Ohguchi, T. Shibayama, S. Watanabe, H. Kinoshita, *J. Nucl. Mater.* 432 (2013) 23–27.
- [32] Y. Zhou, P. Zhang, J. Xiong, F. Yan, *RSC Adv.* 41 (2019) 23589–23597.
- [33] S. Mandal, P.V. Sivaprasad, V. Subramanya Sarma, *Mater. Manuf. Process.* 25 (2010) 54–59.
- [34] Q.N. Song, Y. Tong, H.L. Li, H.N. Zhang, N. Xu, G.Y. Zhang, Y.F. Bao, W. Liu, Z.G. Liu, Y.X. Qiao, *J. Iron Steel Res. Int.* 29 (2022) 359–369.
- [35] Y.B. Tang, X.W. Shen, Z.H. Liu, Y.X. Qiao, L.L. Yang, D.H. Lu, J.S. Zou, J. Xu, *Acta Metall.* 58 (2022) 324–333.
- [36] R. Jiang, G. Zou, W. Shi, Y. Liang, S. Xiang, *J. Mater. Eng. Perform.* 28 (2019) 1863–1872.
- [37] M. Wu, Z. Zhao, X. Wang, C. Wang, P. Liang, *Mater. Corros.* 70 (2019) 461–469.
- [38] Z. Jia, Z.X. Gao, J.J. Ji, D.X. Liu, T.B. Guo, Y.T. Ding, *Materials* 12 (2019) 1900426.
- [39] S. Ningshen, U.K. Mudali, *J. Mater. Eng. Perform.* 19 (2010) 274–281.
- [40] J. Qian, C. Chen, H. Yu, F. Liu, H. Yang, Z. Zhang, *Corros. Sci.* 111 (2016) 352–361.

Springer Nature or its licensor (e.g. a society or other partner) holds exclusive rights to this article under a publishing agreement with the author(s) or other rightsholder(s); author self-archiving of the accepted manuscript version of this article is solely governed by the terms of such publishing agreement and applicable law.